



Impact of aerosol-radiation interaction on new particle formation

Gang Zhao¹, Yishu Zhu¹, Zhijun Wu¹, Taomou Zong¹, Jingchuan Chen¹, Tianyi Tan¹, Haichao Wang¹,
Xin Fang¹, Keding Lu¹, Chunsheng Zhao², Min Hu^{1*}

1 State Key Joint Laboratory of Environmental Simulation and Pollution Control, International Joint
5 Laboratory for Regional Pollution Control, Ministry of Education, College of Environmental Sciences
and Engineering, Peking University, Beijing, 100871, China

2 Department of Atmospheric and Oceanic Sciences, School of Physics, Peking University, Beijing,
100871, China

*Correspondence author: Min Hu (minhu@pku.edu.cn)

10 Abstract

New particle formation (NPF) is thought to contribute to half of the global cloud condensation
nuclei. A better understanding of the NPF at different altitudes can help assess the impact of NPF on
cloud formation and corresponding physical properties. However, NPF is not sufficiently understood
in the upper boundary layer because previous studies mainly focus on ground-level measurements. In
15 this study, the developments of aerosol size distribution at different altitudes are characterized based
on the field measurement conducted in January 2019, in Beijing, China. We find that the partition of
nucleation mode particles at the upper boundary layer is larger than that at the ground, which implies
that the nucleation processing is more likely to happen in the upper boundary layer than that at the



ground. Results of the radiative transfer model show that the photolysis rates of the nitrogen dioxide
20 and ozone increase with altitude within the boundary layer, which lead to a higher concentration of
sulfuric acid at the upper boundary layer than that at the ground. Therefore, the nucleation processing
in the upper boundary layer should be stronger than that at the ground, which is consistent with our
measurement results. Our study emphasizes the influence of aerosol-radiation interaction on the NPF.
These results have the potential to improve our understanding of source of cloud condensation nuclei
25 in global scale due to the impacts of aerosol-radiation interaction.

1 Introduction

Atmospheric particles influence the earth's energy balance by directly interacting with the solar
radiation and indirectly being activated as cloud condensation nucleation (CCN) (Ghan and Schwartz,
2007). New particle formation (NPF) in the atmosphere and the herein coagulation may enable
30 particles to grow larger than 60 nm, at which point aerosols can exert radiative effects on the solar
radiation and act as CCN (Williamson et al., 2019; Shang et al., 2020). Some researchers find that the
NPF is responsible for around half of the global CCN (Merikanto et al., 2009; Du et al., 2017; Kulmala
et al., 2014). However, there is still considerable uncertainty about the magnitude that the NPF attribute
to CCN (Kulmala et al., 2004; Merikanto et al., 2009; Zhang et al., 2012). A better understanding of the
35 NPF at different altitudes can help assess the impact of NPF on cloud formation and corresponding
radiative effects. However, the underlying mechanism of NPF at different altitudes was not well
studied yet.



Nucleation requires sufficient amounts of precursor gases (Kulmala et al., 2004). Sulfuric acid (H_2SO_4) is thought to be the most important precursor for NPF events (Weber et al., 1997, 1996; Weber et al., 2001; Stolzenburg et al., 2005; Kulmala and Markku, 2013). Knowledge in the profile of H_2SO_4 number concentrations ($[H_2SO_4]$) can help understand the NPF mechanism, while the profile of the sulfuric acid is not well known due to the limitation of measurements.

The content of H_2SO_4 in a pseudo-steady state can be calculated (Kulmala et al., 2001) with:

$$[H_2SO_4] = k[OH][SO_2]/CS \quad (1)$$

Where $[OH]$ and $[SO_2]$ are the number concentrations of hydroxyl radical and sulfur dioxide, respectively; CS is the condensation sink, which quantifies the limitation of NPF from existing particles. It is calculated as (Maso et al., 2005):

$$CS = 2\pi D \sum \beta_m(D_{p,i}) D_{p,i} N_i \quad (2)$$

where N_i is the particle concentration in the size $D_{p,i}$. The D is the diffusion coefficient of the H_2SO_4 and the β_m is the transition regime correction factor. The $[OH]$ is related to solar ultraviolet radiation (Rohrer and Berresheim, 2006). Previous studies found that the profile of photolysis radiation varies significantly for different aerosol vertical distributions and the ultraviolet radiation is highly related to the aerosol optical properties (Tao et al., 2014). Therefore, the ambient aerosol-radiation interaction may exert a significant influence on the NPF through determining the $[OH]$ vertical profile. However, the influence of ultraviolet radiation on the NPF is not well understood.



In the past few decades, extensive measurements have been conducted at ground level to characterize the ambient aerosol particle number size distribution (PNSD) and then NPF events (Bullard et al.; Du et al., 2018; Peng et al., 2017; Malinina et al., 2017). Some studies suggest that the nucleation of fine particles can be altitude-dependent (Shang et al., 2018). High concentrations of nucleation-mode particles were found in the upper parts of the boundary layer (Schobesberger et al., 2013). It is observed that the particle growth rate in the upper boundary layer is larger than that on the ground (Du et al., 2017). Measurements from the tethered balloon also show that a large partition of 11-16 nm particles was generated from the top region of the boundary layer, and was then rapidly mixed down throughout the boundary layer (Chen et al., 2018; Platis et al., 2016). Aircrafts measurements (Wang et al., 2016; Zhao et al., 2020) also found that free troposphere favors the NPF. Most of these studies, to our best knowledge, focus on the concentration of precursor gases, but not on the aerosol-radiation interaction.

In this study, we first demonstrate that the NPF is more likely to happen in the upper boundary layer than in the near-ground surface layer based on field measurement of the aerosol PNSD profiles. We find that the tendency of NPF is well related to ultraviolet radiation, implying that the aerosol-radiation interaction is an important factor that influences the NPF.

2 Data and Methods

2.1 Field Measurement



The field measurements were carried from 17 to 19 January 2019 at the Institute of Atmospheric
75 Physics (IAP), Chinese Academy of Sciences (39°18' N, 116°22' E), an urban site in Beijing China.
Details of the measurement site can refer to Wang et al. (2018). Vertical measurements were conducted
from the tower-based platform, with a maximum of 350 m, on the IAP campus. All of the instruments
were installed on a moving cabin of the tower, which moves up and down in altitudes between 0 and
240 m. The cabin moved around 10 meters every minute in altitude. Aerosol PNSD in the size range
80 between 10 nm and 700 nm were measured using a scanning mobility particle size (SMPS; TSI Inc.
3010). Aerosol scattering coefficient (σ_{sca}) at the wavelength of 450 nm, 525 nm, and 635 nm were
measured by an Aurora 3000 nephelometer (Müller et al., 2011). The nitrogen dioxide (NO₂) was
measured based on its absorbance at 405 nm with a low-power lightweight instrument (model 405 nm,
2B Technology, USA). The nitrogen monoxide (NO) was measured by adding an excess of ozone with
85 another power lightweight instrument (model 106-L, 2B Technology, USA). The wind speed, wind
direction, ambient relative humidity, and temperature were measured by a small auto meteorology
station. This instrument can record the atmosphere pressure, which was used to retrieve the altitude
information.

2.2 Lognormal fit of PSND

90 For each of the measured PNSD, it is fitted by three lognormal distribution modes by:

$$N(Dp) = \sum_{i=1,2,3} \frac{N_i}{\sqrt{2\pi} \log(\sigma_{g,i})} \exp \left[-\frac{\log(Dp) - \log(Dp_i)}{2 \log^2(\sigma_{g,i})} \right] \quad (3)$$



Where N_i , $\sigma_{g,i}$, and Dp_i are the number concentration, geometric standard deviation, and geometric mean diameter of mode i respectively. Two examples of fitting the measured PNSD are shown in Fig. S1. The three modes with geometric diameter ranges of 10 ~ 25 nm, 25 ~ 100 nm, and 100 ~ 700 nm
95 correspond to the nucleation mode, Aitken mode, and accumulation mode respectively. The nucleation particles mainly result from the nucleation process and the Aitken mode particles are from primary sources, such as traffic sources (Shang et al., 2018). The accumulation mode particles are correlated with secondary formation, which mainly represents the ambient pollution conditions (Wu et al., 2008).

2.3 Mie Model

100 Mie scattering model (Bohren and Huffman, 2007) is used to estimate the aerosol optical properties. When running the Mie model, aerosol PNSD, aerosol black carbon mass size distribution and refractive index are essential. The measured mean black carbon mass size distribution from Zhao et al. (2019) is adopted in this study, which is measured around 3 kilometers away from this site. The refractive index of the non-black carbon and black carbon aerosol component are $1.64+0i$, which is
105 the measured mean aerosol refractive index measured at Beijing (paper in preparation), and $1.96 + 0.66i$ (Zhao et al., 2017) respectively. The aerosol hygroscopic growth is not considered here because the ambient relative humidity during the measurement was all the way lower than 30% as shown in fig. 1(b). With the measured different aerosol PNSD and above-mentioned information, we can calculate the corresponding aerosol optical properties, which contain the aerosol σ_{sca} , aerosol single
110 scattering albedo (SSA) and asymmetry factor (g).



2.4 TUV Model

The Tropospheric Ultraviolet-Visible radiation model (TUV), developed by Madronich and Flocke (1997), is an advanced transfer model with an eight-stream, discrete ordinate solver. This model can calculate the spectral irradiance, spectral actinic flux, and photo-dissociation frequencies in the wavelength range between 121 nm and 735 nm. In this study, the photolysis frequency of the nitrogen dioxide ($J(\text{NO}_2)$) and ozone ($J(\text{O}^1\text{D})$) were used for further study. Inputs of the TUV model are the aerosol optical depth and single scattering albedo (Tao et al., 2014). The cloud aerosol optical depth is set to be zero in this study. The output of the TUV model includes the profiles of $J(\text{NO}_2)$ and $J(\text{O}^1\text{D})$.

Some changes were made in the source code of the TUV model so that the model can calculate the $J(\text{NO}_2)$ and $J(\text{O}^1\text{D})$ profiles with different aerosol optical profiles (including aerosol σ_{sca} , SSA, and g).

3 Results and Discussions

3.1 Aerosol PNSD at different altitude and time

The measured aerosol PNSD profiles in the time range between 7:00 and 18:50 on January were used for analysis, which contained eight different upward movement and downward movement of the cabin, respectively. Fig. 1 (a) gives detailed time-altitude information of each measurement. All of the time mentioned in the research corresponds to the local time zone.



On January 18, the measured ambient temperature and relative humidity ranges were $-3^{\circ}\text{C} \sim 10^{\circ}\text{C}$ and $13\% \sim 24\%$ respectively, which implied that the ambient air in the winter of Beijing are dry and cold. Aerosol hygroscopic growth was thus not considered in this study. The wind speeds during the measurement were lower than 1m/s , and thus the measurement results of aerosol microphysical properties were hardly influenced by transportation.

During the measurement, the σ_{sca} varied between 0 and 400Mm^{-1} . It ranged between 100Mm^{-1} and 200Mm^{-1} on 18, January. We compared the measured σ_{sca} using the nephelometer and calculated σ_{sca} using the Mie scattering model and measured PNSD. The measured and calculated σ_{sca} show good consistency with slope values of 1.00, 0.95, and 0.89 for wavelengths of 450 nm, 525 nm, and 635 nm, respectively, as shown in Fig. S2. The calculated σ_{sca} values are slightly smaller than that of the measured ones because the measured aerosol PNSD only covers the aerosol diameter between 10 nm and 700 nm, while the measured σ_{sca} represents the optical properties of the whole population. The square of the correlation coefficients are 0.97, 0.97, and 0.97 for the above-mentioned different wavelengths. Our results demonstrate that the measured ambient aerosol PNSDs are reliable for further analysis.

The measured aerosol PNSD varied significantly for different altitudes and a different time. PNSD profiles in Fig. 2 corresponded to these time periods when the cabin moved upward. The corresponding downward PNSD profiles are shown in Fig. S2. In the early morning, the PNSD on the ground surface is substantially different for different altitudes. Particle number concentration on the ground surface



can reach $1.5 \times 10^4 \text{ cm}^{-3}$, and the number concentrations peaked at smaller than 100 nm. It was only $8 \times 10^3 \text{ cm}^{-3}$ with peaking aerosol diameter at around 200 nm at a higher altitude around 200 m. The solar radiation in the morning was very weak, therefore, the turbulence mixing of the aerosol among different altitudes was very weak. The initial emission from the ground surface cannot be mixed up to higher locations, and thus the aerosol number concentrations at the surface was larger than that at a higher level as shown in Fig. 2(a).

With the increment of solar radiation and ambient temperature, the turbulence mixing of ambient particle became stronger. The aerosol PNSD at the surface decreased with time because the near ground particles were mixed up to a higher location as shown in Fig. 2(b) and (c). However, the aerosol PNSD at higher altitude increased with time due to the upcoming mixed aerosol particles from lower altitude. Therefore, the difference between the aerosol PNSD at different altitudes became smaller with the development of the boundary layer as shown in Fig. 2 (b), (c), and (d). These particles were still not well mixed at the range between 0 and 240 m until 11:20.

In the afternoon, the boundary layer was well mixed with the increment of solar radiation and ambient temperature. The aerosol PNSD and PVSD were almost uniformly distributed as shown in Fig. 2 (e) and (f). However, the turbulence was relatively weak after 15:00 as the measured PNSD and PVSD on the ground surface were slightly larger than that of a higher place. After 16:00, the turbulence was weaker because a larger difference between the PNSD at the ground surface and the higher level existed. The ambient particles were hardly mixed after the sunset. The measured aerosol PNSD profiles



showed almost the same properties as that in the morning, with more aerosol particles located on the ground surface from emissions.

Overall, the measured PNSD profiles were highly related to the intensity of turbulence. When the turbulence was weak, the PNSD at surface was different from that of upper levels because the initially emitted particles cannot be mixed up to higher location. The PNSD tended to be uniformly distributed when the turbulence within the boundary layer was strong.

3.2 Nucleation process in the upper boundary layer

We calculated aerosol total number concentration for each measured PNSD (N_{tot}) and the profiles of N_{tot} are shown in Fig. 3 (a). All of the profiles in Fig. 3 corresponded to these cases when the cabin is moving up. The N_{tot} profiles varied significantly with the development of the boundary layer. In the morning, the N_{tot} in the surface (larger than $2 \times 10^4 \text{ cm}^{-3}$) was larger than that at a higher level (lower than $1 \times 10^4 \text{ cm}^{-3}$) because the turbulence is so weak that the initially emitted particles on the surface cannot be transported to the upper level. In the afternoon around 14:00 and 16:00, the aerosol was well mixed in the boundary layer and N_{tot} was almost uniform with around 1.2×10^4 per cubic centimeter. Afterward, the turbulence was weaker than that in the early afternoon and again the emitted aerosols cannot reach the higher level. The profile of N_{tot} in the morning was similar to that in the late afternoon and night.

The number ratio profiles of nucleation mode to Aitken mode (N_1/N_2) for different times are shown in Fig. 3(b) and summarized in Table 1. In the morning of 7:00, the ratio decreased from around



185 0.6 to 0.04 when the cabin moved up from 0 to 240 m. The ratio on the ground surface decreased
because the temperature and turbulence increased when it came to 8:00-10:00 in the morning. However,
the turbulence was not strong enough to mix all of the particles to upper levels to 240 nm. The ratio
still decreased with altitude. In the afternoon, the boundary layer developed well and the ratios between
13:20 and 14:25 were almost uniformly distributed at different altitudes. However, we found that the
190 ratio increased with altitude from 0.21 to 0.34 when it came to 16:15, which implied that more
nucleation mode particles were formed in the upper level in the boundary layer. The increment of the
ratio was hardly influenced by transportation because the wind speed during the measurement was all
the time lower than 1 m/s as shown in Fig. 1(b).

To better configure the variations of PNSD, we calculated the aerosol number concentrations with
195 the diameter between 10 and 25 nm ($N_{10-25\text{nm}}$). The $N_{10-25\text{nm}}$ profiles in Fig. 3(c) show almost the same
trends with the number ratio of N_1 to N_2 . In the morning and later afternoon, the $N_{10-25\text{nm}}$ decreased
with the altitude. The $N_{10-25\text{nm}}$ in the early afternoon were uniformly distributed due to the strong
mixing in the boundary layer. When it came to 16:15, the $N_{10-25\text{nm}}$ at different altitudes were larger
than that in the early afternoon. Most importantly, $N_{10-25\text{nm}}$ increases with altitude. The aerosol total
200 volume at 16:15 does not increase with altitude because the nucleation produced particles are so small
that they contribute negligibly to the aerosol total volume.

Based on the discussion above, we found that the total aerosol number concentrations increased
slightly with altitude at 16:15. The number ratio of N_1 to N_2 and the $N_{10-25\text{nm}}$ increased with altitude.
The total volumes of the aerosol particles were almost the same at different altitudes. The variation of



205 PNSD was hardly influenced by transportation. Therefore, we concluded that the nucleation process was more likely to happen in the upper level of the boundary layer than the ground surface. This phenomenon was not observed in the early afternoon because the turbulence in the early afternoon is so strong that the aerosol particles are well mixed in the boundary layer.

Many previous studies have reported the NPF events in the upper boundary layer. The study in
210 Platis et al. (2016) reported that the NPF originated at elevated altitude, and then being mixed down to the ground in Germany. The higher nucleation mode particle number concentrations were observed at the top region of the boundary layer and were then rapidly mixed throughout the boundary layer in America (Chen et al., 2018). Qi et al. (2019) also found the NPF at the top of the boundary layer based on tethered airship measurements in eastern China. The NPF events were also observed at different
215 altitude in the North China Plain (Zhu et al., 2019).

3.3 Influence of Aerosol-radiation Interaction on NPF

Based on equation 1, the nucleation rate mainly depends on $[OH]$, $[SO_2]$, and CS. The $[SO_2]$ is not available at this measurement. However, we measured the $[NO_x]$, which is the sum of NO and NO_2 . The profiles of the $[SO_2]$ and $[NO_x]$ should be the same because both of them are mainly emitted from
220 the ground and then mixed up by turbulence. The $[NO_x]$ in the afternoon is almost uniformly distributed as shown in Fig. 4(a). Thus, the $[SO_2]$ should be uniformly distributed in the afternoon within the boundary layer. The CS profiles, in Fig. 4(b), were almost uniformly distributed in the afternoon. Therefore, the $[OH]$ is the only main factor that may result in different characteristics of



NPF at different altitudes. Based on the work of Ehhalt and Rohrer (2000), the [OH] can be calculated
225 by:

$$[OH] = a[J(O^1D)]^\alpha [J(NO_2)]^\beta \frac{b[NO_2]+1}{c[NO_2]^2+d[NO_2]+1} \quad (4)$$

With α , β , a , b , c , d equaling 0.83, 0.19, 4.1×10^9 , 140, 0.41, and 1.7, respectively. From equation 4,
the vertical distribution of $J(O^1D)$, and $J(NO_2)$ played a significant influence on [OH] and further
influence the NPF. However, the $J(O^1D)$, and $J(NO_2)$ were not measured. The TUV model was
230 employed to estimate the $J(O^1D)$, and $J(NO_2)$ for different aerosol profiles.

The input of the TUV needs the aerosol optical properties in the altitude range between 0-20 km.
The parameterization of aerosol number concentration profiles by Liu et al. (2009) with aircraft
measurement in Beijing is used in this study. Liu et al. (2009) found that number concentration constant
within the boundary layer, linearly decreasing within the transition layer and exponential decreasing
235 above the transition layer, when the particles within the boundary are well mixed. The normalized
aerosol PNSD (PNSD divided by total aerosol number concentration) was assumed to be the same at
different altitudes. The BC to total aerosol mass concentration ratio was also assumed to be the same
at different altitudes (Ferrero et al., 2011). The σ_{sca} , SSA, and g profiles can be calculated by Mie
theory under these assumptions (Zhao et al., 2017; Zhao et al., 2018).

240 The lines with squares in Fig. 5(a) and (b) provide the calculated photolysis rates of $J(O^1D)$, and
 $J(NO_2)$ with a boundary layer altitude of 1000 m. Results show that both the $J(O^1D)$, and $J(NO_2)$
increase with altitude within the boundary layer. The $J(O^1D)$ increases from $8.9 \times 10^{-3} \text{ s}^{-1}$ to 14.3×10^{-3}



$^3 \text{ s}^{-1}$ and $J(\text{NO}_2)$ increases from $3.0 \times 10^{-5} \text{ s}^{-1}$ to $6.2 \times 10^{-5} \text{ s}^{-1}$ in the boundary layer. The corresponding [OH] increased from $6.2 \times 10^6 \text{ cm}^{-3}$ to $11.9 \times 10^6 \text{ cm}^{-3}$ based equation 4. Thus, the [OH] at the top of the boundary layer is two times of that on the ground surface due to the variation in photolysis rate. Our estimated [OH] at the surface is consistent with the previously estimated relationships between the [OH] and $J(O^1D)$ (Rohrer and Berresheim, 2006).

Overall, the aerosol profiles tend to be uniformly distributed within the boundary layer due to the strong turbulence in the afternoon. The corresponding estimated $J(O^1D)$, and $J(\text{NO}_2)$ values increase with altitude, which leads to higher [OH] at the top of the boundary layer than that at the ground. Therefore, the $[\text{H}_2\text{SO}_4]$ should increase with altitude based on equation 1. There should be more nucleation processing at the top of the boundary layer than that at the ground, which is consistent with our field measurement. The schematic graph of the influence of aerosol-radiation interaction on NPF is shown in Fig. 6.

3.4 Impact of Boundary layer development on the photolysis rates

For a better understanding of the aerosol-radiation interaction on NPF, we estimated the photolysis rates under different aerosol vertical profiles. Based on the work of Liu et al. (2009), two typical types of aerosol profiles exists under different boundary layer as shown in Fig. S4. For the first type of boundary layer, aerosols were not well mixed within the boundary layer and the aerosol number concentrations decrease with altitude exponentially (type A). Another type of boundary layer has aerosol number concentration constant in the boundary layer and then decreasing with altitude above



the boundary (type B). For type B, we estimated the corresponding photolysis rate for different boundary layer heights between 500 m and 1000 m, which covers the mean boundary layer altitude in the North China Plain (Zhu et al., 2018). The different aerosol optical depth (AOD), which ranges
265 between 0.3 and 2, are used for different pollution conditions.

Four different aerosol profiles are used in this study. Details of the four different aerosol profiles are summarized in Table 2. The first one corresponds to the aerosol boundary layer type A, with a boundary altitude of 1000 m and AOD of 0.3 (B1). The second aerosol profile has the same boundary altitude of 1000m and AOD of 0.3, but the boundary layer type is changed into B (B2). The third
270 aerosol profile also corresponds to boundary layer type B, and a boundary layer altitude of 1000m, but the AOD is 0.8 (B3). The last one has a boundary layer altitude of 500m, with an AOD of 0.8 and a boundary layer type of B (B4).

The $J(O^1D)$, and $J(NO_2)$ profiles under the above-mentioned aerosol profiles are estimated and shown in Fig. 5 (a) and (b). For each type, both the $J(O^1D)$, and $J(NO_2)$ increase with altitude. The
275 increased ratio of the $J(O^1D)$ with altitude (k_{O^1D}) are 1.7×10^{-5} , 2.0×10^{-5} , 3.0×10^{-5} , and $5.4 \times 10^{-5} \text{ s}^{-1} \text{ km}^{-1}$, for the aerosol profile of B1, B2, B3, and B4 respectively. The corresponding increase ratio of the $J(NO_2)$ with altitude (k_{NO_2}) are 2.6×10^{-3} , 3.3×10^{-3} , 5.3×10^{-3} , and $9.0 \times 10^{-3} \text{ s}^{-1} \text{ km}^{-1}$, for B1, B2, B3, and B4, respectively. The increase ratio of [OH] were estimated to be 3.4×10^6 , 4.1×10^6 , 5.5×10^6 , and $7.4 \times 10^6 \text{ cm}^{-3} \text{ km}^{-1}$ for B1, B2, B3 and B4, respectively (Table 2).



280 These four profiles represent the typical ambient aerosol profiles in the early morning, late
morning, early afternoon, and late afternoon, respectively. In the early morning, the turbulence in the
boundary layer is weak and the aerosol within the boundary layer is not well mixed (B1). In the late
morning, the aerosol in the boundary is well mixed and uniformly distributed due to the increasing
turbulence (B2). The early afternoon (B3) should have higher AOD when compared with that in the
285 late morning due to the formation of the secondary aerosol. However, the boundary layer altitude
decreased in the late afternoon (B4) because the turbulence within the boundary layer weakened
compared with B3. The ambient aerosol profiles tend to change from B1 to B4 from early morning to
late afternoon. The corresponding k_{O^1D} and k_{NO_2} increased with the development of the boundary
layer. In the late afternoon, the difference of photolysis rate at the top of the boundary layer and ground
290 are largest. Furthermore, the turbulence in the mixing layer is weakened and the nucleation formed
particles cannot be mixed down to the ground. Therefore, it is more likely to observe more nucleation
mode particles at the top of the boundary layer than at the ground in the late afternoon, which is
consistent with our measurement.

4. Conclusion

295 In this study, we characterized the aerosol PNSD at different times and different altitudes based
on field measurements at a urban site, in Beijing, China. Our measurements show that the aerosol size
distribution profiles varied significantly with the development of the boundary layer.



In the morning, the turbulence in the boundary was weak and the initial emitted particles cannot be mixed to a higher layer. The corresponding aerosol PNSD at the surface was larger than that at
300 higher locations. At noon, the particles within the boundary were well mixed and tend to be uniformly distributed at different altitudes. In the late afternoon, we found more nucleation mode particles at a higher altitude than that at the ground. The larger partitions of nucleation mode particles do not result from transformation. We concluded that the nucleation processing in the upper boundary layer were more likely to happen than that at the ground.

305 The TUV model was employed to estimate the profile of photolysis rate for different aerosol profiles. Results showed that both the $J(O^1D)$, and $J(NO_2)$ values increased with altitude, which led to higher [OH] at the top of the boundary layer than that at the ground. The corresponding [H₂SO₄] should increase with altitude based on equation 1, when the aerosol was well mixed and uniformed in the mixed layer. Therefore, more nucleation processing at the top of the boundary layer may happen
310 than that at the ground, which is consistent with our field measurement.

We also estimate the corresponding photolysis rate profile under different boundary structures. The increasing ratio of the photolysis rate with altitude increase with the development of the boundary layer from early morning to late afternoon. In the late afternoon, the difference of the photolysis rate at the upper boundary layer and that at the ground are the largest. At the same time, the turbulence is
315 not so strong that the nucleation mode particles formed in the upper boundary layer are not able to mix down to the ground. Therefore, it is a favor to observe higher nucleation mode particles concentration at the upper boundary layer than that at the ground in the afternoon. Our study reveals that the vertical



distribution of ambient aerosols would first influence the vertical profile of the photolysis rate. Then the NPF for different altitudes is tuned due to the different photolysis rates.

320

Data availability. The data is available upon request to the corresponding author.

Author contributions. Gang Zhao and Yishu Zhu did the analysis and wrote the manuscript. Min Hu, Chunsheng Zhao, Zhijun Wu, Xin Fang, and Gang Zhao discussed the results. Yishu Zhu, Jingchuan Chen, Taomou Zong, Tianyi Tan, Keding Lu, and Haichao Wang conducted the measurements.

325 **Competing interests.** The authors declare that they have no conflict of interest.

Acknowledgments. This work is supported by the National Natural Science Foundation of China (91844301) and the National Key Research and Development Program of China (2016YFC0202000 Task 3, 5).

330



References

- Bohren, C. F., and Huffman, D. R.: Absorption and Scattering by a Sphere, in: Absorption and Scattering of Light by Small Particles, Wiley-VCH Verlag GmbH, 82-129, 2007.
- Bullard, R. L., Singh, A., Anderson, S. M., Lehmann, C. M. B., and Stanier, C. O.: 10-Month
335 characterization of the aerosol number size distribution and related air quality and meteorology at the Bondville, IL Midwestern background site, Atmospheric Environment, <http://dx.doi.org/10.1016/j.atmosenv.2016.12.055>.
- Chen, H., Hodshire, A. L., Ortega, J., Greenberg, J., McMurry, P. H., Carlton, A. G., Pierce, J. R., Hanson, D. R., and Smith, J. N.: Vertically resolved concentration and liquid water content of
340 atmospheric nanoparticles at the US DOE Southern Great Plains site, Atmospheric Chemistry and Physics, 18, 311-326, 10.5194/acp-18-311-2018, 2018.
- Du, P., Gui, H., Zhang, J., Liu, J., Yu, T., Wang, J., Cheng, Y., and Shi, Z.: Number size distribution of atmospheric particles in a suburban Beijing in the summer and winter of 2015, Atmospheric Environment, 186, 32-44, 10.1016/j.atmosenv.2018.05.023, 2018.
- 345 Du, W., Zhao, J., Wang, Y., Zhang, Y., Wang, Q., Xu, W., Chen, C., Han, T., Zhang, F., Li, Z., Fu, P., Li, J., Wang, Z., and Sun, Y.: Simultaneous measurements of particle number size distributions at ground level and 260 m on a meteorological tower in urban Beijing, China, Atmos. Chem. Phys., 17, 6797-6811, 10.5194/acp-17-6797-2017, 2017.
- Ehhalt, D. H., and Rohrer, F.: Dependence of the OH concentration on solar UV, Journal of
350 Geophysical Research: Atmospheres, 105, 3565-3571, <https://doi.org/10.1029/1999JD901070>, 2000.
- Ferrero, L., Mocnik, G., Ferrini, B. S., Perrone, M. G., Sangiorgi, G., and Bolzacchini, E.: Vertical profiles of aerosol absorption coefficient from micro-Aethalometer data and Mie calculation over Milan, Science of the Total Environment, 409, 2824-2837, 2011.
- Ghan, S. J., and Schwartz, S. E.: Aerosol Properties and Processes: A Path from Field and Laboratory
355 Measurements to Global Climate Models, Bulletin of the American Meteorological Society, 88, 1059-1084, 10.1175/bams-88-7-1059, 2007.
- Kulmala, and Markku: Direct Observations of Atmospheric Aerosol Nucleation, Science, 2013.



- 360 Kulmala, M., Maso, M. D., Mäkelä J. M., Pirjola, L., Väkevä M., Aalto, P., Määttä, P., Hämeri, K., and O’Dowd, C. D.: On the formation, growth and composition of nucleation mode particles, *Tellus B: Chemical and Physical Meteorology*, 53, 479-490, 10.3402/tellusb.v53i4.16622, 2001.
- Kulmala, M., Vehkamäki, H., Petaja, T., Dal Maso, M., Lauri, A., Kerminen, V. M., Birmili, W., and McMurry, P. H.: Formation and growth rates of ultrafine atmospheric particles: a review of observations, *Journal of Aerosol Science*, 35, 143-176, 10.1016/j.jaerosci.2003.10.003, 2004.
- 365 Kulmala, M., Petäjä T., Ehn, M., Thornton, J., Sipilä M., Worsnop, D. R., and Kerminen, V. M.: Chemistry of Atmospheric Nucleation: On the Recent Advances on Precursor Characterization and Atmospheric Cluster Composition in Connection with Atmospheric New Particle Formation, *Annual Review of Physical Chemistry*, 65, 21-37, 10.1146/annurev-physchem-040412-110014, 2014.
- Liu, P., Zhao, C., Zhang, Q., Deng, Z., Huang, M., Xincheng, M. A., and Tie, X.: Aircraft study of aerosol vertical distributions over Beijing and their optical properties, *Tellus Series B-Chemical &*
370 *Physical Meteorology*, 61, 756–767, 2009.
- Madronich, S., and Flocke, S.: Theoretical Estimation of Biologically Effective UV Radiation at the Earth’s Surface, in: *Solar Ultraviolet Radiation*, Berlin, Heidelberg, 1997, 23-48.
- Malinina, E., Rozanov, A., Rozanov, V., Liebing, P., Bovensmann, H., and Burrows, J. P.: Aerosol particle size distribution in the stratosphere retrieved from SCIAMACHY limb measurements,
375 *Atmospheric Measurement Techniques Discussions*, 1-29, 10.5194/amt-2017-388, 2017.
- Maso, M. D., Kulmala, M., Riipinen, I., Wagner, R., Hussein, T., Aalto, P. P., and Lehtinen, K. E. J.: Formation and growth of fresh atmospheric aerosols: eight years of aerosol size distribution data from SMEAR II, Hyytiälä, Finland, *Boreal Environment Research*, 10, 323-336, 2005.
- Merikanto, J., Spracklen, D. V., Mann, G. W., Pickering, S. J., and Carslaw, K. S.: Impact of nucleation
380 on global CCN, *Atmospheric Chemistry and Physics*, 9, 8601-8616, 10.5194/acp-9-8601-2009, 2009.
- Müller, T., Laborde, M., Kassell, G., and Wiedensohler, A.: Design and performance of a three-wavelength LED-based total scatter and backscatter integrating nephelometer, *Atmos. Meas. Tech.*, 4, 1291-1303, 10.5194/amt-4-1291-2011, 2011.



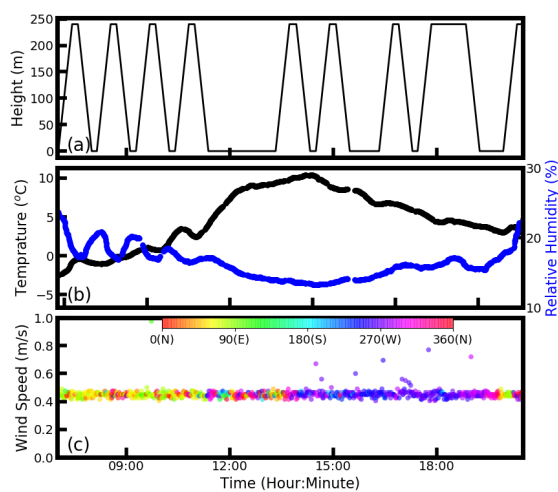
- Peng, Y., Liu, X., Dai, J., Wang, Z., Dong, Z., Dong, Y., Chen, C., Li, X., Zhao, N., and Fan, C.:
385 Aerosol size distribution and new particle formation events in the suburb of Xi'an, northwest China,
Atmospheric Environment, 153, 194-205, 10.1016/j.atmosenv.2017.01.022, 2017.
- Platis, A., Altstatter, B., Wehner, B., Wildmann, N., Lampert, A., Hermann, M., Birmili, W., and
Bange, J.: An Observational Case Study on the Influence of Atmospheric Boundary-Layer Dynamics
on New Particle Formation, Boundary-Layer Meteorology, 158, 67-92, 10.1007/s10546-015-0084-y,
390 2016.
- Qi, X., Ding, A., Nie, W., Chi, X., Huang, X., Xu, Z., Wang, T., Wang, Z., Wang, J., Sun, P., Zhang,
Q., Huo, J., Wang, D., Bian, Q., Zhou, L., Zhang, Q., Ning, Z., Fei, D., Xiu, G., and Fu, Q.: Direct
measurement of new particle formation based on tethered airship around the top of the planetary
boundary layer in eastern China, Atmospheric Environment, 209, 92-101,
395 10.1016/j.atmosenv.2019.04.024, 2019.
- Rohrer, F., and Berresheim, H.: Strong correlation between levels of tropospheric hydroxyl radicals
and solar ultraviolet radiation, Nature, 442, 184-187, 10.1038/nature04924, 2006.
- Schobesberger, S., Vaananen, R., and Leino, K.: Airborne measurements over the boreal forest of
southern Finland during new particle formation events in 2009 and 2010, Boreal Environment
400 Research, 2013.
- Shang, D., Hu, M., Zheng, J., Qin, Y., Du, Z., Li, M., Fang, J., Peng, J., Wu, Y., Lu, S., and Guo, S.:
Particle number size distribution and new particle formation under the influence of biomass burning
at a high altitude background site at Mt. Yulong (3410 m), China, Atmospheric Chemistry and Physics,
18, 15687-15703, 10.5194/acp-18-15687-2018, 2018.
- 405 Shang, D., Peng, J., Guo, S., Wu, Z., and Hu, M.: Secondary aerosol formation in winter haze over the
Beijing-Tianjin-Hebei Region, China, Frontiers of Environmental Science & Engineering, 15,
10.1007/s11783-020-1326-x, 2020.
- Stolzenburg, M. R., McMurry, P. H., Sakurai, H., Smith, J. N., Mauldin III, R. L., Eisele, F. L., and
Clement, C. F.: Growth rates of freshly nucleated atmospheric particles in Atlanta, Journal of
410 Geophysical Research: Atmospheres, 110, <https://doi.org/10.1029/2005JD005935>, 2005.



- Tao, J. C., Zhao, C. S., Ma, N., and Liu, P. F.: The impact of aerosol hygroscopic growth on the single-scattering albedo and its application on the NO₂ photolysis rate coefficient, *Atmos. Chem. Phys.*, 14, 12055-12067, 10.5194/acp-14-12055-2014, 2014.
- Wang, H., Lu, K., Chen, X., Zhu, Q., Wu, Z., Wu, Y., and Sun, K.: Fast particulate nitrate formation via N₂O₅ uptake aloft in winter in Beijing, *Atmospheric Chemistry and Physics*, 18, 10483-10495, 10.5194/acp-18-10483-2018, 2018.
- Wang, J., Krejci, R., Giangrande, S., Kuang, C., Barbosa, H. M., Brito, J., Carbone, S., Chi, X., Comstock, J., Ditas, F., Lavric, J., Manninen, H. E., Mei, F., Moran-Zuloaga, D., Pohlker, C., Pohlker, M. L., Saturno, J., Schmid, B., Souza, R. A., Springston, S. R., Tomlinson, J. M., Toto, T., Walter, D., Wimmer, D., Smith, J. N., Kulmala, M., Machado, L. A., Artaxo, P., Andreae, M. O., Petaja, T., and Martin, S. T.: Amazon boundary layer aerosol concentration sustained by vertical transport during rainfall, *Nature*, 539, 416-419, 10.1038/nature19819, 2016.
- Weber, R. J., Marti, J. J., McMurry, P. H., Eisele, F. L., Tanner, D. J., and Jefferson, A.: MEASURED ATMOSPHERIC NEW PARTICLE FORMATION RATES: IMPLICATIONS FOR NUCLEATION MECHANISMS, *Chemical Engineering Communications*, 151, 53-64, 10.1080/00986449608936541, 1996.
- Weber, R. J., Marti, J. J., McMurry, P. H., Eisele, F. L., Tanner, D. J., and Jefferson, A.: Measurements of new particle formation and ultrafine particle growth rates at a clean continental site, *Journal of Geophysical Research: Atmospheres*, 102, 4375-4385, <https://doi.org/10.1029/96JD03656>, 1997.
- Weber, R. J., Chen, G., Davis, D. D., Mauldin, R. L., Tanner, D. J., Eisele, F. L., Clarke, A. D., Thornton, D. C., and Bandy, A. R.: Measurements of enhanced H₂SO₄ and 3-4 nm particles near a frontal cloud during the First Aerosol Characterization Experiment (ACE 1), *J Geophys Res-Atmos*, 106, 24107-24117, 10.1029/2000jd000109, 2001.
- Williamson, C. J., Kupc, A., Axisa, D., Bilsback, K. R., Bui, T., Campuzano-Jost, P., Dollner, M., Froyd, K. D., Hodshire, A. L., Jimenez, J. L., Kodros, J. K., Luo, G., Murphy, D. M., Nault, B. A., Ray, E. A., Weinzierl, B., Wilson, J. C., Yu, F., Yu, P., Pierce, J. R., and Brock, C. A.: A large source

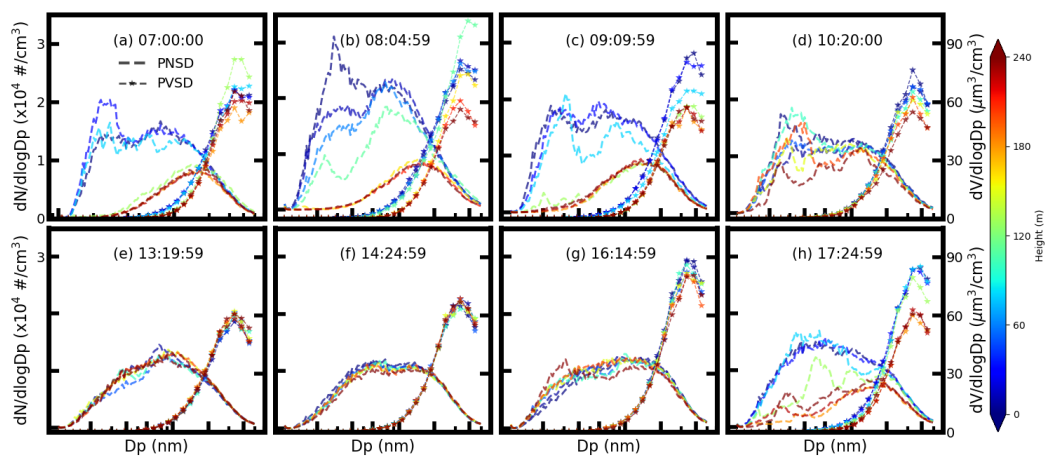


- of cloud condensation nuclei from new particle formation in the tropics, *Nature*, 574, 399-403, 10.1038/s41586-019-1638-9, 2019.
- 440 Wu, Z., Hu, M., Lin, P., Liu, S., Wehner, B., and Wiedensohler, A.: Particle number size distribution in the urban atmosphere of Beijing, China, *Atmospheric Environment*, 42, 7967-7980, <https://doi.org/10.1016/j.atmosenv.2008.06.022>, 2008.
- Zhang, R. Y., Khalizov, A., Wang, L., Hu, M., and Xu, W.: Nucleation and Growth of Nanoparticles in the Atmosphere, *Chemical Reviews*, 112, 1957-2011, 10.1021/cr2001756, 2012.
- 445 Zhao, B., Shrivastava, M., Donahue, N. M., Gordon, H., Schervish, M., Shilling, J. E., Zaveri, R. A., Wang, J., Andreae, M. O., Zhao, C., Gaudet, B., Liu, Y., Fan, J., and Fast, J. D.: High concentration of ultrafine particles in the Amazon free troposphere produced by organic new particle formation, *Proceedings of the National Academy of Sciences*, 117, 25344, 10.1073/pnas.2006716117, 2020.
- 450 Zhao, G., Zhao, C., Kuang, Y., Tao, J., Tan, W., Bian, Y., Li, J., and Li, C.: Impact of aerosol hygroscopic growth on retrieving aerosol extinction coefficient profiles from elastic-backscatter lidar signals, *Atmospheric Chemistry and Physics*, 17, 12133-12143, 10.5194/acp-17-12133-2017, 2017.
- Zhao, G., Zhao, C., Kuang, Y., Bian, Y., Tao, J., Shen, C., and Yu, Y.: Calculating the aerosol asymmetry factor based on measurements from the humidified nephelometer system, *Atmospheric Chemistry and Physics*, 18, 9049-9060, 10.5194/acp-18-9049-2018, 2018.
- 455 Zhao, G., Tao, J., Kuang, Y., Shen, C., Yu, Y., and Zhao, C.: Role of black carbon mass size distribution in the direct aerosol radiative forcing, *Atmos. Chem. Phys.*, 19, 13175-13188, 10.5194/acp-19-13175-2019, 2019.
- Zhu, X., Tang, G., Guo, J., Hu, B., Song, T., Wang, L., Xin, J., Gao, W., M ünkel, C., Sch äfer, K., Li, X., and Wang, Y.: Mixing layer height on the North China Plain and meteorological evidence of serious air pollution in southern Hebei, *Atmospheric Chemistry and Physics*, 18, 4897-4910, 460 10.5194/acp-18-4897-2018, 2018.
- Zhu, Y., Wu, Z., Park, Y., Fan, X., Bai, D., Zong, P., Qin, B., Cai, X., and Ahn, K. H.: Measurements of atmospheric aerosol vertical distribution above North China Plain using hexacopter, *Sci Total Environ*, 665, 1095-1102, 10.1016/j.scitotenv.2019.02.100, 2019.

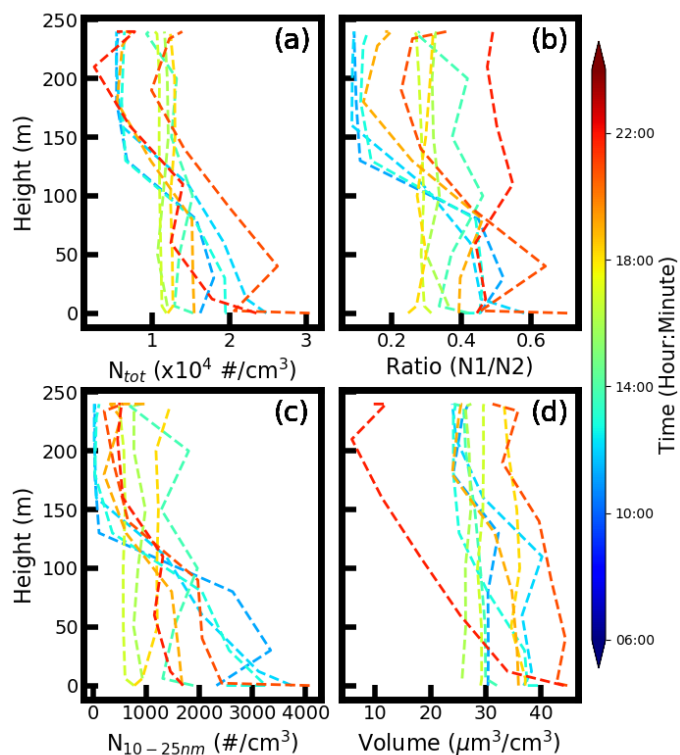


465

Figure 1. Time series of (a) the measurement altitude, (b) temperature (black line) and relative humidity (blue line), and (c) the wind speed and wind direction.



470 **Figure 2.** The measured aerosol PSND (dashed line) and the PVSD (dashed line with star) at (a) 7:00,
(b) 8:05, (c) 9:50, (d) 10:20, (e) 13:20, (f) 14:25, (g) 16:15, and (h) 17:25. The filled colors represent
the corresponding measurement altitude above the ground.



475 **Figure 3.** The measured (a) aerosol number concentrations, (b) number ratio of the nucleation mode aerosol number concentrations to Aitken mode aerosol number concentrations, (c) aerosol number concentrations for 10-25 nm, and (d) measured aerosol volume concentrations at different altitudes. The filled colors of different lines denote the different measurement times.

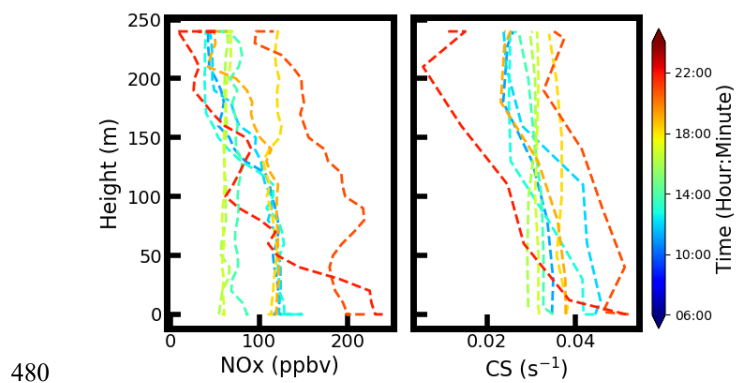
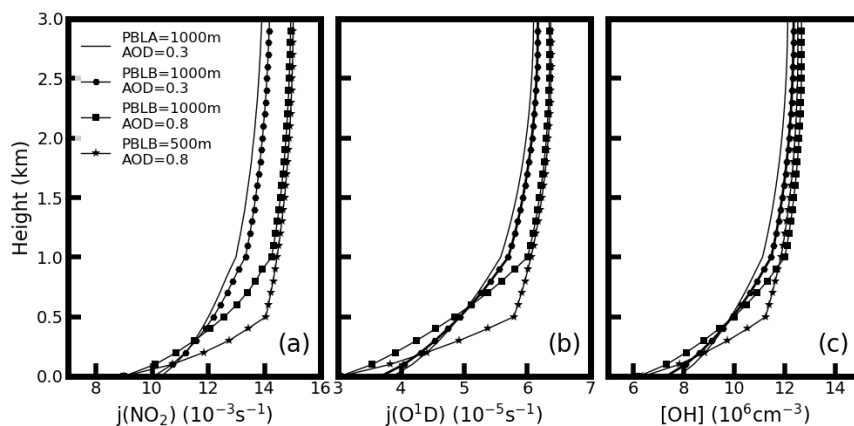
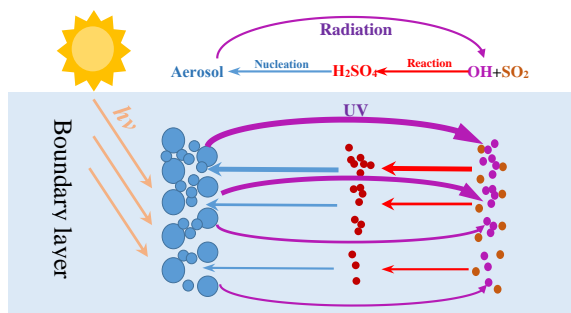


Figure. 4. The measured (a) NO_x and (b) CS at different altitudes. The filled colors of different lines denote the different measurement times.



485 **Figure 5.** The estimated (a) $j(\text{NO}_2)$, (b) $j(\text{O}^1\text{D})$, and (c) OH concentration for different aerosol profiles.

The (1) solid line, (2) solid line marked with hexagon, (3) solid line marked with squares, and (4) solid line marked with stars represent the aerosol distribution of B1, B2, B3, and B4, respectively.



490 **Figure 6.** Schematic of the influence of aerosol-radiation interaction on NPF.

495



500

Table 1. The number ratio of nucleation mode to Aiken mode.

Time Altitude	7:00	8:05	9:10	10:20	13:20	14:25	16:15	17:25
0	0.56	0.52	0.43	0.36	0.21	0.20	0.21	0.32
30	0.63	0.44	0.42	0.35	0.21	0.19	0.23	0.30
60	0.61	0.34	0.40	0.40	0.22	0.19	0.27	0.28
110	0.05	0.26	0.25	0.46	0.27	0.19	0.28	0.14
160	0.04	0.03	0.07	0.39	0.20	0.17	0.27	0.17
210	0.03	0.03	0.08	0.51	0.20	0.17	0.30	0.31 ⁵⁰⁵
240	0.04	0.03	0.09	0.26	0.21	0.16	0.34	0.37



Table 2. Details of the aerosol optical profiles and estimated photolysis values.

Profile	Type ^{*1}	Altitude ^{*2}	AOD	k [J(NO ₂)] (10 ⁻³ s ⁻¹ km ⁻¹)	k [J(O ¹ D)] (10 ⁻⁵ s ⁻¹ km ⁻¹)	k [OH] (10 ⁶ cm ⁻³ km ⁻¹)
B1	A	1000	0.3	2.6	1.7	3.4
B2	B	1000	0.3	3.3	2.0	4.1
B3	B	1000	0.8	5.3	3.0	5.5
B4	B	500	0.8	9.0	5.4	7.4

^{*1}Boundary layer Type.

510 ^{*2}Boundary layer altitude.